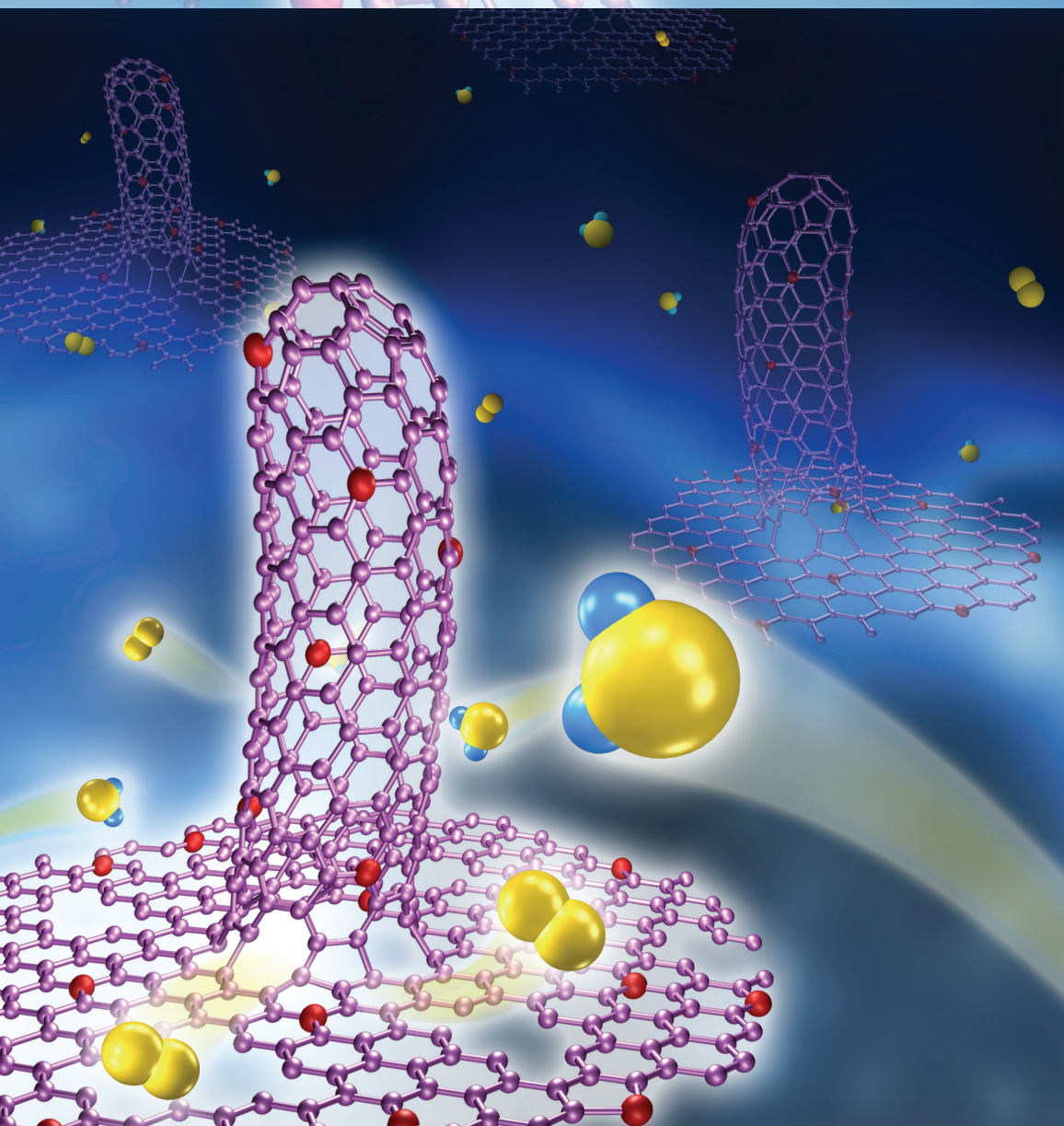


Volume 10 · No. 11 – June 12 2014

NANO | MICRO

small

www.small-journal.com



11/2014

WILEY-VCH

Special Issue: Graphene Research in China

Nitrogen-Doped Graphene/Carbon Nanotube Hybrids: In Situ Formation on Bifunctional Catalysts and Their Superior Electrocatalytic Activity for Oxygen Evolution/Reduction Reaction

Gui-Li Tian, Meng-Qiang Zhao, Dingshan Yu, Xiang-Yi Kong, Jia-Qi Huang, Qiang Zhang,* and Fei Wei*

There is a growing interest in oxygen electrode catalysts for oxygen reduction reaction (ORR) and oxygen evolution reaction (OER), as they play a key role in a wide range of renewable energy technologies such as fuel cells, metal-air batteries, and water splitting. Nevertheless, the development of highly-active bifunctional catalysts at low cost for both ORR and OER still remains a huge challenge. Herein, we report a new N-doped graphene/single-walled carbon nanotube (SWCNT) hybrid (NGSH) material as an efficient noble-metal-free bifunctional electrocatalyst for both ORR and OER. NGSHs were fabricated by in situ doping during chemical vapor deposition growth on layered double hydroxide derived bifunctional catalysts. Our one-step approach not only provides simultaneous growth of graphene and SWCNTs, leading to the formation of three dimensional interconnected network, but also brings the intrinsic dispersion of graphene and carbon nanotubes and the dispersion of N-containing functional groups within a highly conductive scaffold. Thus, the NGSHs possess a large specific surface area of $812.9 \text{ m}^2 \text{ g}^{-1}$ and high electrical conductivity of 53.8 S cm^{-1} . Despite of relatively low nitrogen content (0.53 at%), the NGSHs demonstrate a high ORR activity, much superior to two constituent components and even comparable to the commercial 20 wt% Pt/C catalysts with much better durability and resistance to crossover effect. The same hybrid material also presents high catalytic activity towards OER, rendering them high-performance cheap catalysts for both ORR and OER. Our result opens up new avenues for energy conversion technologies based on earth-abundant, scalable, noble-metal-free catalysts.

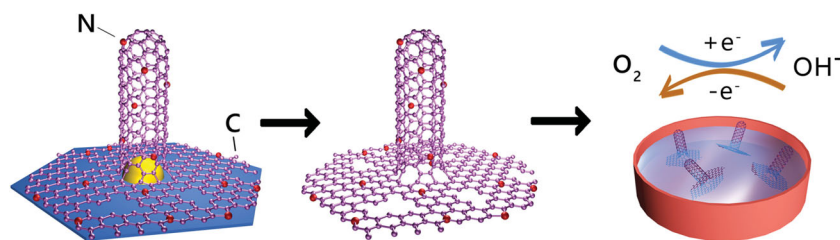
G.-L. Tian, Dr. M.-Q. Zhao, X.-Y. Kong, Dr. J.-Q. Huang, Prof. Q. Zhang, Prof. F. Wei
Beijing Key Laboratory of Green Chemical Reaction Engineering and Technology
Department of Chemical Engineering
Tsinghua University
Beijing 100084, P. R. China
E-mail: zhang-qiang@mails.tsinghua.edu.cn; wf-dce@tsinghua.edu.cn
Dr. D. S. Yu
School of Chemical and Biomedical Engineering
Nanyang Technological University
62 Nanyang Drive
Singapore 637459, Singapore



DOI: 10.1002/sml.201303715

1. Introduction

The chemical energy from unrenewable fossil fuels brings the flourish of our society, however, the vast energy consumption induces the rapid depletion of traditional fossil fuels and increasingly worsens environmental pollution. High-capacity energy systems (e.g. fuel cells, metal-air batteries) are highly desirable to meet the urgent requirement of electric vehicles and utilization of sustainable energies.^[1] Oxygen electrode catalysts for oxygen reduction reaction (ORR) and oxygen evolution reaction (OER) are at the heart in a wide range of renewable energy technologies such as fuel cells, metal-air batteries, and water splitting. The ORR is the ubiquitous cathodes



Scheme 1. One step growth of nitrogen doped graphene/carbon nanotube hybrids for oxygen reduction and oxygen evolution reaction.

reaction in fuel cells and metal-air batteries and the current bottleneck for fuel cells lies in the sluggish kinetics of ORR, which causes severe energy efficiency loss. The platinum and its alloy are known to be very efficient in boosting the ORR rate. Nevertheless, their high cost and poor stability hinder their industrialization and Pt has only moderate activity for the OER, which is the anode reaction and plays a key role in energy conversion and storage such as solar fuel synthesis and rechargeable metal-air batteries.^[2–4] Ruthenium (Ru) and iridium (Ir) oxides have been usually used to expedite the OER reaction, which suffer from the scarcity and high cost of the precious metals and are not as active for the ORR as Pt. A bifunctional catalyst for both reactions could be employed in a unitized regenerative fuel cell (URFC), a promising energy storage device which works as a fuel cell and in reverse as a water electrolyzer to feed the fuel cell. Therefore, it is highly concerned to develop highly active bifunctional catalysts at low cost for both ORR and OER to replace conventional notable metals.

The heteroatom-doped nanocarbon materials as a noble-metal-free electrocatalyst for ORR have attracted great attentions attributed to their low cost, high electrocatalytic activity and selectivity, as well as excellent durability.^[5,6] Very recently, nitrogen-doped carbon nanomaterials were used as an efficient oxygen evolution electrocatalyst,^[4] indicating that the heteroatom-doped nanocarbon materials may act as a bifunctional electrocatalyst for the oxygen electrochemistry. However, as for the two typical nanocarbon materials, one-dimensional (1D) CNTs and two-dimensional (2D) graphene nanosheets, both of them are inclined to aggregate or stack with each other due to the strong van der Waals forces, which hinders the full utilization of the active sites for catalytic reactions.

The integration of graphene and CNTs into a hybrid material is quite a promising strategy to enhance the dispersion of graphene and CNTs, to inherit the advantages of both graphene and CNTs, and to obtain an efficient and effective electronic and thermal conductive three dimensional (3D) network.^[7,8] The post-organization routes by a facile mixing,^[9] liquid phase reaction,^[10] hydrothermal synthesis,^[11] layer-by-layer self-assembly,^[12] and self assembly at the liquid/air interface,^[13] are effective and scalable to obtain graphene/CNT (G/CNT) hybrids. The use of a unique oxidation condition to unzip the outer walls of the few-walled CNTs can create nanographene attached to the inner tubes.^[14] The as-obtained hybrids contain extremely small amount of iron residuals originated from nanotube growth seeds and nitrogen impurities that facilitate the formation of

catalytic sites and boost the ORR activity of the catalyst.^[14] A facile hydrothermal process under mild conditions was employed to obtain nitrogen-doped graphene/CNT nanocomposite that exhibited synergistically enhanced electrochemical activity for the ORR.^[15] However, the construction of effective connection especially for covalent C-C bonding between graphene and CNTs, which is important to overcome the interface

problems and fully demonstrate the properties of G/CNT hybrids, is extremely complex. The use of chemical vapor deposition (CVD) for the fabrication of G/CNT hybrids is more attractive due to its ability to provide the possibility for the covalent C-C bonding between graphene and CNTs and to prepare G/CNT hybrids with various kinds of structures.^[16,17] If heteroatoms can be directly introduced into the framework of such hybrids, the as-obtained heteroatom-doped nanocarbon would not only be a promising catalyst candidate for oxygen electrochemical reaction but also aid novel material platform to elucidate the correlation between the structure, composition, and electrocatalytic activity of heteroatom-doped nanocarbon.

In this contribution, we reported the fabrication of novel N-doped graphene/single-walled CNT hybrids (NGSHs) by in situ doping during catalytic CVD growth. The reason we select graphene and SWCNTs as the building blocks is that single-layer graphene and SWCNTs are considered as the high end for nanocarbon technology because they are with much better intrinsic properties when compared with multi-layer graphene and multi-walled CNTs (MWCNTs), such as higher specific surface area (SSA), lower defect density, and tunable electronic characteristics according to their edge/chirality.^[18] However, the nitrogen-containing functional groups are very difficult to be grafted on graphene and SWCNTs by post treatment because of the ultra-high crystallization and very low defect density.^[19] Based on these considerations, in situ CVD in which the nitrogen source was simultaneously introduced with carbon source was employed to dope the graphene/SWCNT hybrids (GSHs) for one-step catalytic synthesis of NGSHs. The as-obtained NGSHs, together with GSHs were employed as efficient noble-metal-free electrocatalysts for OER and ORR.

2. Results and Discussion

2.1. Catalytic Growth of NGSHs on Bifunctional Catalysts

The **Scheme 1** illustrated the in situ formation of NGSHs on flake catalysts. Layered double hydroxides (LDHs), which are a kind of hydroxalite-like materials composed of positively-charged layers and charge-balancing inter-layer anions, are employed as the bifunctional catalysts for NGSH formation. The reason we selected LDHs as the catalysts is that most metals can be arranged on the atomic level in a lamellar LDH flake with controllable components.^[20] As a result, similar to the graphene formation on

MgO,^[21] Al₂O₃,^[22] and SiO₂,^[23] the layered double oxide (LDO) plates (mainly MgO and Mg₂Al₂O₄ phase at a high temperature of 950 °C^[24]) derived from LDHs at high temperature can be used as the oxide catalysts for graphene formation. Meanwhile, the tiny Fe-containing nanoparticles (NPs) embedded on such plates can be available with tunable size and controllable composition for CNT growth, which is quite important for SWCNT growth that requires ultra-fine and stable reduced metal NPs.^[25] Therefore, the FeMoMgAl LDHs were employed as the catalyst precursors for the growth of GSHs and NGSHs. As shown in Figure S1, the as-fabricated FeMoMgAl LDHs were hexagonal flakes with a lateral size of 1–2 μm and a thickness of tens of nanometers. After calcination, the well-crystallized LDHs were converted to the corresponding LDO flakes with the plate-like structure retaining, which were mainly composed of MgO, Fe₃O₄, and MgAl₂O₄. The well-preserved lamellar LDO flakes were effective templates for the CVD growth of graphene layers with the introduction of methane as carbon source at 950 °C. Meanwhile, the induced hydrogen from the cracking of methane reduced the LDOs and led to the formation of well-dispersed Fe NPs. With the pinning effect of Mo,^[25] the as-produced Fe NPs were with high thermal stability and tunable size distribution of 1–5 nm. The methane was catalytically decomposed on these Fe NPs for SWCNT formation. During the CVD, NH₃ was introduced as the nitrogen source to induce the doping of N functional groups, leading to the formation of NGSH/LDO nanocomposites (Figure 1a–c). Note that the deposition of porous N-doped graphene and the synchronously growth of SWCNTs happened on both sides of the LDO flakes due to that the embedded Fe NPs were found on both sides of one LDO flake (Figure 1d). Figure 1c illustrated an Fe NP at the interface of the NGSHs between a SWCNT and graphene. An extra ring-like graphene layer was detected at the tip of a baby SWCNT, which was different from the situation when only SWCNTs were grown on the LDO flakes and can be considered as the intrinsic characteristics for a covalent C–C bonding between graphene and SWCNTs.^[7,17] GSHs were produced for comparison using the similar CVD method without the introduction of NH₃.

2.2. Nanostructures of the NGSHs

After the removal of LDO flakes, the NGSHs were available. As shown in Figure 1d–f, the interlinked morphology of NGSHs was similar to the pristine NGSH/LDO nanocomposites. The tips of the SWCNTs were connected to the graphene layers closely, as shown in the high resolution TEM images (Figure 1e,f). Note that the LDH precursor was calcined and reduced at a temperature as high as 950 °C, under which atoms in a diffusion couple (such as Mg–Al, Mg–Fe) were with different diffusivities. As a result, a supersaturation of lattice vacancies emerged and led to a condensation of extra vacancies in the form of Kirkendall voids.^[24] The Kirkendall effect induced pores distributed on the corresponding LDO flakes, which consequently brought about the pores with the width of several nanometers to tens of nanometers

in the graphene layers, as illustrated in Figure 1e & 1f. There was also sp² carbon deposited in the mesopores as graphene protuberances. After the removal of template catalysts, the flake morphology was well casted by the unstacking double-layer graphene, in which the graphene protuberances acted as the spacers to prevent the stacking of the graphene layers deposited on the both sides of flakes. The pore size distribution of the NGSHs was calculated from N₂ sorption isotherm (Figure S2a) based on the density functional theory (DFT) model. Compared with GSHs, the NGSHs exhibited a larger total pore volume of 2.233 cm³ g⁻¹. There are mainly micropores of ca. 1 nm and mesopores of ca. 4.5 nm on NGSHs (Figure S2b). The SSA of NGSHs calculated by the multipoint Brunauer–Emmett–Teller (BET) method was 812.9 m² g⁻¹, much larger than that of GSHs (565.6 m² g⁻¹). A very strong C1s peak can be available on the full peak of X-ray photoelectron spectroscopy (XPS). The content and configurations of the doped nitrogen were identified by N1s peak deconvolution (Figure 1g). The analysis showed that the total content of nitrogen heteroatoms in the NGSH was 0.58 at.%. The N atoms were bonded to the surrounding C atoms in pyridinic N (0.13 at.%), pyrrolic N (0.15 at.%), quaternary N (0.15 at.%), oxidized N (0.07 at.%), and chemisorbed N (0.08 at.%), with the bonding energy at 398.7, 400.0, 401.1, 403.1, and 404.8 eV,^[26] respectively. Although the nitrogen content is less than 1 at.%, the doping of N into the carbon scaffolds significantly improved electrocatalytic performance, which will be discussed later in detail. The Raman spectrum presented in Figure S3 showed a bunch of strong radical breathing mode (RBM) peaks, indicating the existence of SWCNTs. The I_D/I_G ratio of NGSHs was 0.12. The detailed structure features of NGSHs and GSHs were summarized in Table 1.

2.3. The Electrocatalytic Activity of NGSHs for OER and ORR

The high graphitic degree, large SSA, abundant porosity, nitrogen heteroatom doping, and unique hybrid structure of NGSHs can contribute a lot to their high electrical conductivity, fast mass transport, large number of active sites, and excellent structural stability, which rendered the NGSHs promising electrocatalytic activity. Herein, the electrocatalytic activity towards ORR and OER was investigated to evaluate the electrocatalytic properties of NGSHs using a three-electrode chemical station with a piece of platinum foil as the counter electrode and a saturated calomel electrode (SCE) as the reference electrode. The potential scale was calibrated to a reversible hydrogen electrode (RHE).

2.3.1. OER Activity of NGSH Electro-Catalysts

The electrocatalytic OER activity of NGSHs was evaluated in a three-electrode system by polarization experiments with the potential extended to the water oxidation regime (from 1.00 to 1.77 V). In 0.1 mol L⁻¹ KOH solution, the NGSH electrode displays much higher OER current than the undoped GSH electrode, while the current on the commercial Pt/C electrode is quite faint by comparison. The

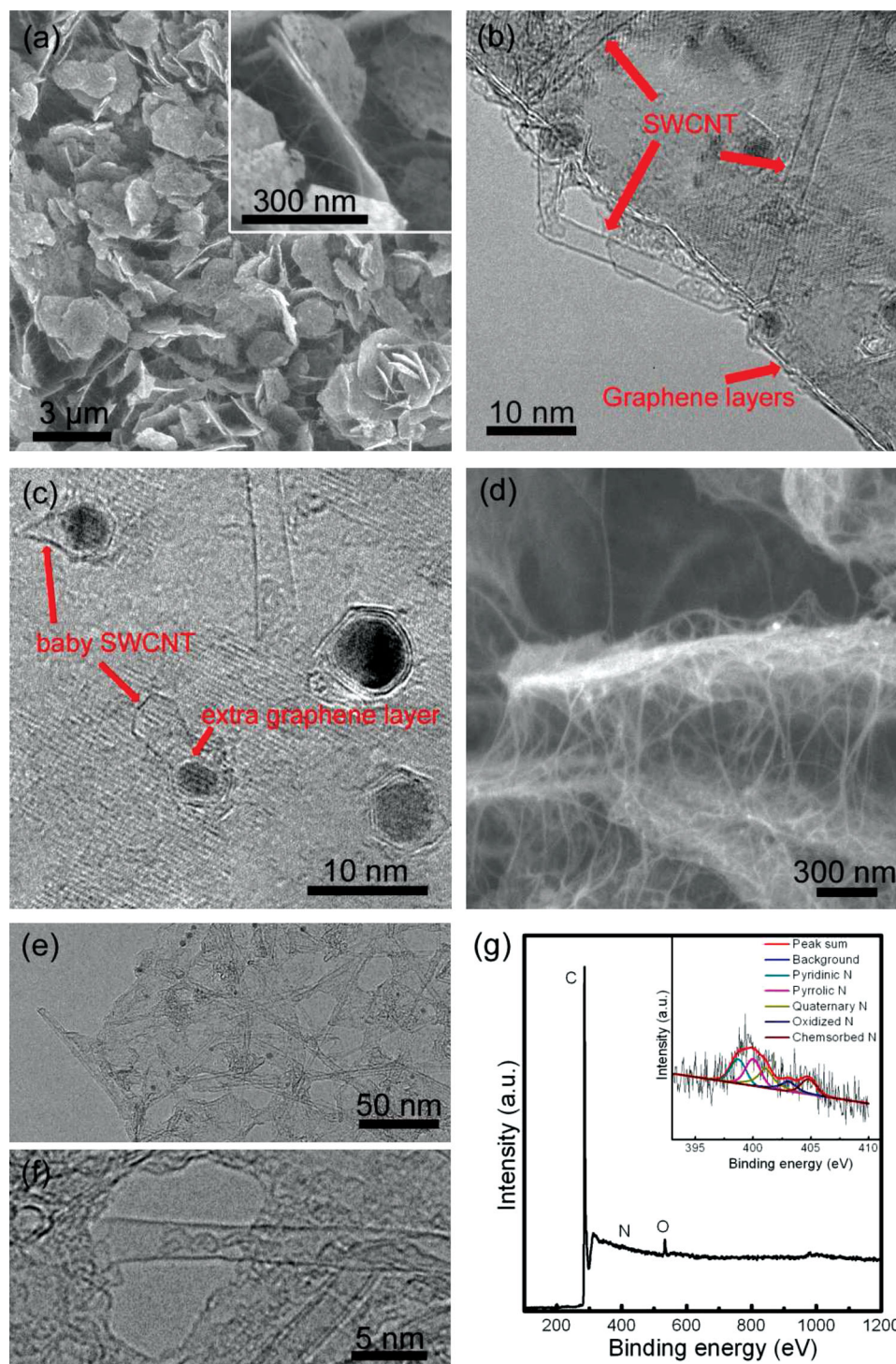


Figure 1. (a) SEM, (b) TEM and (c) high resolution TEM images of the NGSHs on catalysts; The inserted figure in (a) shows one catalyst flake with deposited graphene and SWCNTs. (d) SEM, (e) TEM and (f) high resolution TEM images of the NGSHs; (g) XPS spectrum of the NGSHs; The inset exhibits the high-resolution N 1s spectra.

potential required to oxidize water at the current density of 10 mA cm^{-2} is commonly used to judge the OER activity, which is a metric relevant to solar fuel synthesis.^[2,4] As shown in **Figure 2a**, the NGSH catalyst promoted the OER current density to 10 mA cm^{-2} at a potential of 1.63 V, similar to that of IrO_2/C materials.^[4] In contrast, the undoped GSH catalyst afforded a current density of 10 mA cm^{-2} at an overpotential

$\sim 110 \text{ mV}$ higher than that of NGSHs, implying the superior OER activity of NGSHs due to the nitrogen doping. As for Pt/C, the potential acquired for the current density of 10 mA cm^{-2} would be much more positive deduced from the corresponding current trend. The Tafel slope for the NGSH catalyst was about 83 mV/decade (Figure 2b), much smaller than that of the undoped GSHs (97 mV/decade) and the

Table 1. Summary of structure features of the undoped and nitrogen doped hybrid materials.

Sample	SSA (m ² g ⁻¹)	I _b /I _g	Pore volume (cm ³ g ⁻¹)		Electrical conductivity (S cm ⁻¹)
			micropore	mesopore	
GSHs	565.6	0.19	0	2.202	38.4
NGSHs	812.9	0.12	0.087	2.146	53.8

commercial Pt/C (288 mV/decade), which further confirmed the superior electrocatalytic OER performance of NGSHs.

2.3.2. ORR Activity of NGSH Electro-Catalysts

Figure 3a presented the cyclic voltammograms (CVs) of NGSHs supported glassy carbon electrode in 0.1 mol L⁻¹ KOH solution saturated with N₂ or O₂ at a scan rate of 100 mV s⁻¹. For comparison, CV profiles of the GSH electrode were presented in Figure S4a. In the N₂-saturated solution, featureless voltammetric currents within the potential range between -0.03 and +1.17 V can be observed either for NGSH or GSH samples. In contrast, both of the two hybrid electrode materials demonstrated well-defined cathodic peaks for O₂ reduction when the electrolyte solution was saturated with O₂. The onset potential for Pt/C catalyst in our work is 0.96 V vs. RHE (0.032 V vs. Ag/AgCl/KCl (3M)), which is comparable to the results reported by Qiao et al (0.033 V vs. Ag/AgCl/KCl (3M)).^[27] The onset potential of the ORR on NGSH electrode was more positive and the current density was much higher compared with that on the GSH electrode, indicating the electrocatalytic performance of the GSHs was obviously improved by nitrogen doping in spite of the low doping amount.

In order to explore the ORR mechanism on the NGSH and GSH electrodes, both rotating disk electrode (RDE) and rotating ring-disk electrode (RRDE) characterizations were carried out. The linear sweep voltammetric profiles in Figure 3b,c and Figure S4b showed that the current density was enhanced by increasing the rotating rate. The onset potential of NGSH electrode for ORR was at 0.88 V approximately, close to that identified from the CV measurements (0.86 V), which was about 30 mV more positive than that of the GSH electrode. The corresponding Koutecky-Levich equations of the two samples were calculated to analyze the kinetic parameters for ORR process. Take 0.47 V for an example, the electron transfer numbers of NGSH and GSH electrode based on the slope of the K-L plots (J⁻¹ vs. ω^{-1/2}) were 3.22 and 2.49, respectively (Figure 3d). The corresponding kinetic-limiting current density of the NGSHs was 132.8 mA cm⁻², almost six times higher than that of the undoped ones (23.0 mA cm⁻²). This result may be attributed to the high graphitic degree, large surface area, and abundant porosity of NGSHs, which led to the rapid electron transfer. The RRDE technique was applied to further verify the ORR pathway

and to determine the HO₂⁻ generation rate. Figure 3e showed the curves of current densities vs. the potential at the disk and ring electrode. It is clearly illustrated that the ring current for HO₂⁻ oxidation was much depressed due to the nitrogen doping of the NGSHs. For instance, the amount of HO₂⁻ generated is ca. 34.7% and 73.0% for NGSH electrode and GSH electrode at 0.47 V, respectively (see Figure 3f), and the calculated n value is 3.3 for NGSH and 2.5 for GSH. Both sets of results suggested the much enhanced electrocatalytic performance of NGSHs compared with GSHs.

Furthermore, the electrocatalytic ORR properties of NGSHs and the GSHs were compared with commercial Pt/C (20 wt% platinum on Vulcan XC-72R) catalyst. The same amount of each catalyst by mass (254.8 μg cm⁻²) was loaded onto a RDE. Figure 3c presented the rotating-disk voltammograms in O₂-saturated 0.1 mol L⁻¹ KOH solution at a rotating rate of 1225 rpm. The RDE with GSHs showed a two-step process for ORR with the onset potential at 0.85 and 0.43 V, indicating that the ORR on the GSH electrode favored a two-electron pathway. In contrast, those for the NGSH electrode and Pt/C electrode were one-step process with the onset potential at 0.88 and 0.96 V, respectively, while the current density for NGSH electrode surpassed that for Pt/C electrode at high overpotential. These results indicated that the NGSHs were promising ORR catalysts. To demonstrate the importance of the CNT introduction into the hybrid, a control sample of nitrogen doped graphene with a nitrogen content of 2.31 wt% was available by similar CVD growth on LDO flakes. The current density on the nitrogen doped graphene electrode was -6.43 mA cm⁻², corresponding to -1.09 mA μg_N⁻¹ at 0.47 V vs RHE, which was comparable with that for NG-1^[29] and much lower than that for NGSHs. Moreover, we compared the electrocatalytic ORR activity of NGSHs with other N-doped or B/N co-doped nanocarbons reported in the literatures^[14,28-31] as

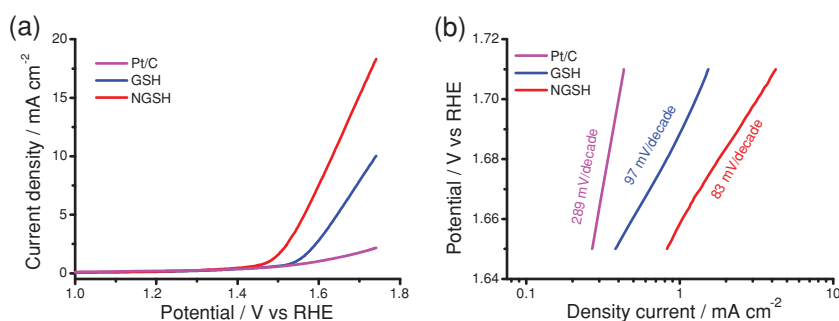


Figure 2. (a) OER currents of Pt/C, GSH, and NGSH electrodes in 0.1 mol L⁻¹ KOH solution at a scan rate of 5 mV s⁻¹. (b) Tafel plots of commercial Pt/C, GSH, and NGSH catalysts recorded at 1 mV s⁻¹ in 0.1 mol L⁻¹ KOH.

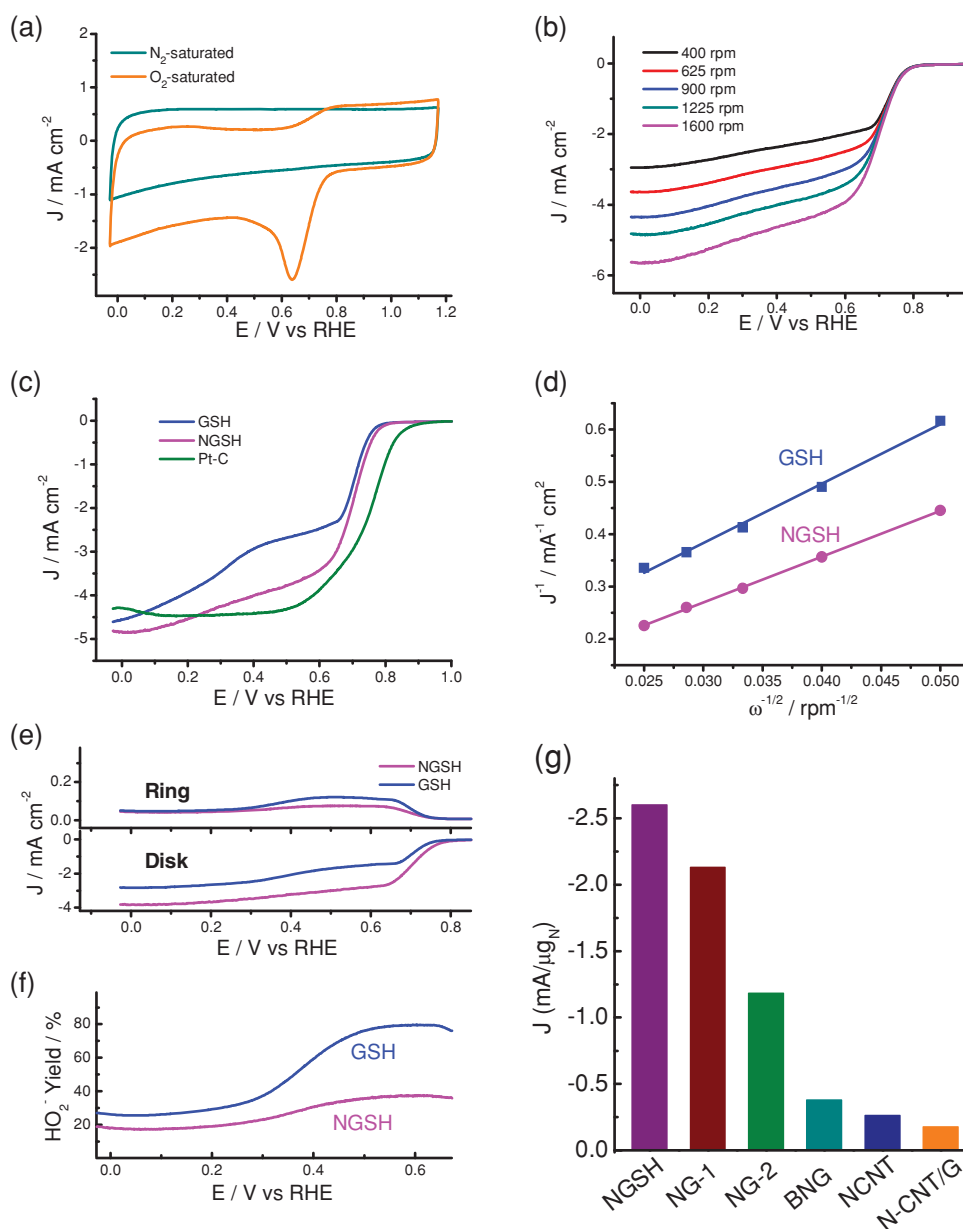


Figure 3. (a) Cyclic voltammograms of the GSHs and the NGSHs on a glassy-carbon RDE electrode in an O_2 -saturated or N_2 -saturated 0.1 mol L^{-1} KOH solution. (b) Rotating-disk voltammograms recorded for NGSHs supported on a GC electrode in an O_2 -saturated 0.1 mol L^{-1} KOH solution at a scan rate of 10 mV s^{-1} with different rotating rates. (c) RDE voltammograms of GSHs, NGSHs and Pt/C supported on GC electrodes at a rotating rate of 1225 rpm with the same experimental conditions as in (a). (d) Koutecky-Levich plot of J^{-1} versus $\omega^{-1/2}$ for GSHs and NGSHs at 0.47 V . (e) Disk current densities (bottom) and the corresponding ring current densities (top) of GSHs and NGSHs on RRDE with a consistent rotating rate of 1225 rpm in O_2 -saturated 0.1 mol L^{-1} KOH solution. (f) The percentage of peroxide of the hybrid catalysts at various potentials. (g) The comparison of electrocatalytic ORR activity on a family of nitrogen doped nanocarbons. The potential of 0.47 V was taken as an example. Data source: NGSH: our results; NG-1: Ref. [28]; NG-2: Ref. [29]; BNG: Ref. [30]; NCNT: Ref. [31]; N-CNT/G: Ref. [14]. The rotating rate was 1600 rpm except that for the BNG electrode which was 1500 rpm . Note that the current densities for the NG-1, NG-2, and NCNT were estimated by the atomic percent instead of mass percent which were higher than the corresponding actual values.

presented in Figure 3g. With the amount of nitrogen atoms doped in the nanocarbons normalized, the current density on the NGSH electrode ($2.6 \text{ mA } \mu\text{g}_N^{-1}$) was much higher than the other doped nanocarbons (including the N-doped graphene,^[28–30] N-doped CNTs,^[31] and N-doped CNT/graphene hybrids^[14]). The NGSHs exhibit an electrical conductivity of 53.8 S cm^{-1} , which is higher than that of GSHs (38.4 S cm^{-1}), and much higher than that of nitrogen doped multi-wall

CNTs ($2\text{--}60 \times 10^{-3} \text{ S cm}^{-1}$)^[32] and reduced graphene oxides ($2.48 \times 10^{-5} \text{ S cm}^{-1}$).^[33] The hybridization of SWCNTs and graphene brings the intrinsic dispersion of each phase, and the doped N atoms are well dispersed at the single sp^2 carbon layers. Therefore, the activity originated from the doping of N^[6,28–30,34] together with contribution from the tiny residual Fe/N/C,^[14,35] can be shown at the interfaces between the electro-catalysts and electrolyte. The quite high electrical

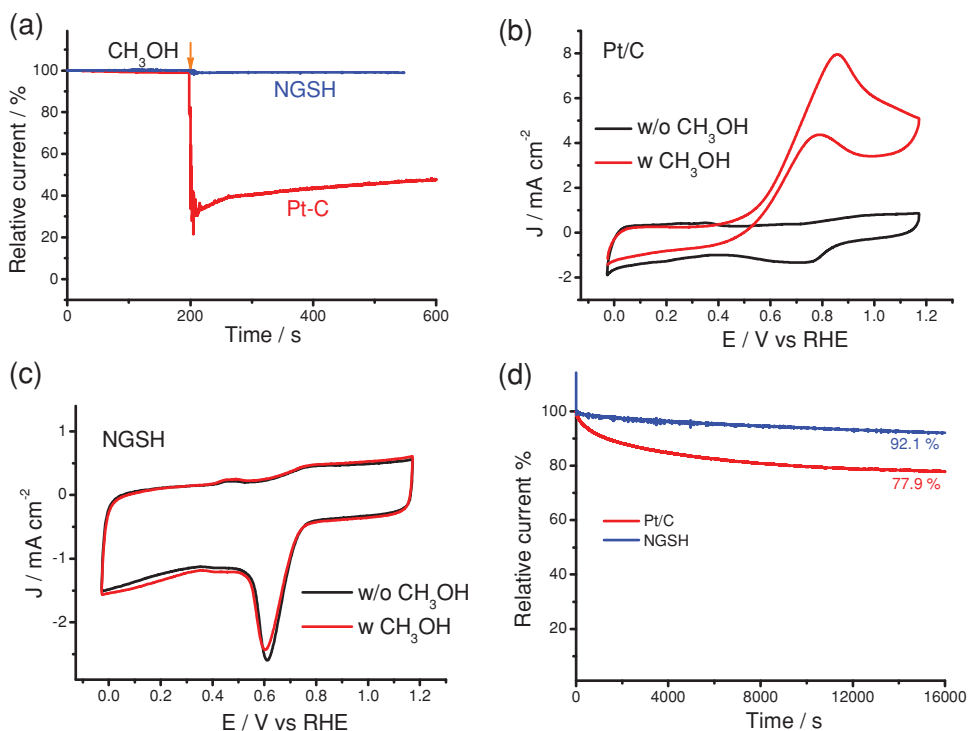


Figure 4. (a) Chronoamperometric response of NGSHs and Pt/C at 0.67 V in O_2 -saturated 0.1 mol L^{-1} KOH solution. The arrows indicate the addition of methanol. CVs of (b) Pt/C and (c) NGSHs electrodes in O_2 -saturated 0.1 mol L^{-1} KOH solution before and after the addition of methanol. (d) Durability evaluation of NGSHs and Pt/C at 0.67 V for 16000 s with a rotating rate of 1600 rpm.

conductivity of NGSHs guarantees the full collection of the current originated from the catalytic reaction. Consequently, the intrinsic dispersed, high conductive NGSHs afford a quite high ORR reactivity.

The electrochemical stability and the possible crossover effect are important issues for cathode materials in fuel cells. As presented in **Figure 4a**, the current-time (i-t) chronoamperometric response for the ORR on Pt/C electrode illustrated a significant decrease in current density upon the addition of methanol (the resulting methanol concentration was 3 mol L^{-1}). In contrast, no conspicuous change was detected in the current density on the NGSH electrode. CVs in O_2 -saturated 0.1 mol L^{-1} KOH solution before and after the addition of methanol confirmed the poor tolerance to methanol of Pt/C electrode (Figure 4b) and the excellent resistance to crossover effects of the NGSH electrode (Figure 4c), since the cathodic peak for ORR had vanished and one pair of anodic peaks, at 0.86 and 0.77 V, were observed for the oxidation of methanol in the CV curve of Pt/C electrode after the addition of methanol, whereas no noticeable change in the CV curve of NGSH electrode under the same conditions. Additionally, chronoamperometric durability tests were also performed at a constant voltage of 0.67 V in a 0.1 mol L^{-1} KOH solution saturated with O_2 at a rotating rate of 1600 rpm (Figure 4d). Remarkably, continuous O_2 reduction on the NGSH electrode resulted high relative current of 92.1% still persisting after 16 000 s. In contrast, the Pt/C electrode showed a current loss as high as 22.1% measured after 16000 s. This result suggested that the durability of NGSHs is superior to that of the Pt/C catalyst. The higher stability of NGSHs is ascribed to the stable covalent

C-N bonds in the framework and that the inert carbon based materials do not suffer activity degradation due to the agglomeration of Pt NPs as Pt/C does.

3. Conclusion

We have demonstrated the synthesis of novel NGSHs by a facile and cost-favorable one-step CVD method. The FeMo-MgAl LDHs derived bifunctional catalysts embedded with thermally stable Fe NPs not only served as an efficient catalyst for the growth of N-doped SWCNTs, but also supplied a lamellar substrate for the templated deposition of N-doped graphene. The as-fabricated NGSHs possess not only large surface area with high porosity but also high graphitic degree. They demonstrate a high ORR activity, much superior to two constituent components and even comparable to the commercial 20 wt% Pt/C catalysts with much better durability and resistance to crossover effect. We also demonstrate that such hybrids have excellent bifunctional oxygen electrode activity for both ORR and OER. This indicates the potential application of NGSHs as a bifunctional electrocatalyst for the regenerative fuel cells and/or rechargeable metal-air batteries involving oxygen electrochemistry. More potential applications may arise if the enhanced electrical and optical properties of doped graphene/CNT hybrids, as opposed to random graphene and/or CNTs, were fully exploited. This work also provides a structural platform toward the design of 3D interconnect materials with extraordinary electron pathways as well as tunable surface/interface that can be used in areas, such as catalysis, separation, drug delivery, energy conversion and storage.

4. Experimental Section

Catalyst Preparation: The FeMoMgAl LDH flakes were synthesized using a urea assisted co-precipitation reaction.^[25,36] $\text{Mg}(\text{NO}_3)_2 \cdot 6\text{H}_2\text{O}$, $\text{Al}(\text{NO}_3)_3 \cdot 9\text{H}_2\text{O}$, $\text{Fe}(\text{NO}_3)_3 \cdot 9\text{H}_2\text{O}$, and $\text{Na}_2\text{MoO}_4 \cdot 2\text{H}_2\text{O}$ were dissolved in 1000 mL deionized water with $[\text{Mg}^{2+}] + [\text{Al}^{3+}] + [\text{Fe}^{3+}] = 0.155 \text{ mol L}^{-1}$, $n(\text{Mg}) : n(\text{Al}) : n(\text{Fe}) : n(\text{Mo}) = 2 : 1 : 0.1 : 0.017$. The urea was then dissolved in the solution with a molar concentration of 3.0 mol L^{-1} . The as-obtained solution was kept at 100°C under continuous magnetic stirring for 9.0 h in a 2000 mL flask, which was equipped with a reflux condenser in ambient atmosphere. The as-obtained suspension was kept at 94°C for another 12 h without stirring. After filtering, washing and freeze-drying, the final products of FeMoMgAl LDH catalysts were available.

Synthesis of N-doped SWCNT/Graphene Hybrids (NGSHs): The NGSHs were prepared using a high-temperature catalytic CVD with FeMoMgAl LDH flakes as the catalyst precursors and ethylene/ammonia as carbon/nitrogen feedstocks. In detail, about 0.5 g LDHs were distributed uniformly on a quartz boat which was then placed at the center of a horizontal quartz tube. The reactor was then inserted into a furnace at atmosphere pressure which was heated to 950°C under flowing Ar (500 mL min^{-1}). When reaching the reaction temperature, the flow rate of Ar was turned down to 200 mL min^{-1} and the mixed gas ($\text{C}_2\text{H}_4/\text{H}_2/\text{NH}_3$) was introduced into the reactor with a flow rate of $300/50/100 \text{ mL min}^{-1}$. The CVD growth was maintained for 15 min at 950°C before the furnace was cooled to room temperature under Ar protection.

The as-obtained products were treated with an NaOH (12.0 mol L^{-1}) aqueous solution at 150°C for 12 h and HCl (5.0 mol L^{-1}) aqueous solution at 80°C for 6 h, subsequently, to remove the FeMoMgAl LDO flakes. The residual Fe was removed by CO_2 oxidation at 900°C and post-acid treatment.^[37] The as-obtained products were filtered, washed, and freeze-dried for further characterization.

Structural Characterizations: The morphology of the LDH flakes and the as-grown N-SGH products were characterized using a JSM 7401F scanning electron microscope (SEM) operated at 3.0 kV and a JEM 2010 high-resolution transmission electron microscope (TEM) operated at 120.0 kV. The Raman spectra were collected with He-Ne laser excitation at 633 nm using Horiba Jobin Yvon LabRAM HR800 Raman spectrophotometer. The thermogravimetric analysis (TGA) was carried out using Mettler Toledo TGA/DSC-1 under O_2 atmosphere. The Brunauer–Emmett–Teller (BET) SSA of the samples were measured by N_2 adsorption/desorption at liquid- N_2 temperature using Autosorb-IQ2-MP-C system. The amounts of N-containing functional groups on NGSH were determined using X-ray photoelectron spectroscopy (XPS) by Escalab 250xi.

Electrocatalytic Performance Measurements: All electrochemical measurements were performed in a three-electrode setup, in which a platinum sheet electrode served as the counter electrode, and a saturated calomel electrode (SCE) served as the reference electrode. The potential scale was calibrated to a reversible hydrogen electrode (RHE). RHE calibration was performed at the end of each characterization in a high pure hydrogen saturated electrolyte with platinum nanoparticles (20 wt% platinum on Vulcan XC-72R) at the working electrode. CVs were run at a scan rate of 1.0 mV s^{-1} , and the average of the two potentials at which the current crossed zero was taken as the thermodynamic potential for the hydrogen electrode reactions. The fabrication

of working electrodes was carried out as follows: taking NGSHs as an example, the catalyst was first ultrasonically dispersed in ethanol (5 mg mL^{-1}). $10 \mu\text{L}$ of aqueous catalyst solution dispersion was then transferred onto the glass carbon electrode (GC, 0.19625 cm^2) via a controlled drop casting approach. After solvent evaporation for 10 min in air, a thin layer of Nafion solution (5 wt% water solution) was coated onto the electrode surface and then dried in an oven setting at 60°C for 30 min to serve as the working electrode.

The measurements were carried out in a 0.1 mol L^{-1} KOH aqueous electrolyte at room temperature. As for ORR experiment, a flow of O_2 or N_2 was maintained over the electrolyte during the recording of electrochemical measurements in order to ensure its continued O_2 or N_2 saturation. Cyclic voltammograms (CVs), linear sweep voltammograms (LSVs), and rotating disk electrode (RDE) tests were carried out using a glassy carbon rotating disk electrode. The scan rate of CVs was kept as 100 mV s^{-1} while 10 mV s^{-1} for LSVs and RDE tests. The OER activities of all the samples were investigated by the LSV method at the scan rate of 5 mV s^{-1} and the Tafel plots were carried out at 1.0 mV s^{-1} . The data were recording using a Solartron 1470E electrochemical station equipped with a 1455A FRA module.

The overall electron transfer numbers per oxygen molecule involved in a typical ORR process can be calculated from the slopes of Koutecky-Levich plots using the following equations:

$$\frac{1}{j} = \frac{1}{j_k} + \frac{1}{j_L} = \frac{1}{j_k} + \frac{1}{B\omega^{1/2}} \quad (1)$$

$$B = 0.62nFC_0D_0^{2/3}\nu^{1/6} \quad (2)$$

$$j_k = nFkC_0 \quad (3)$$

where j is the measured current density, j_k and j_L are the kinetic and diffusion-limiting current densities, ω is the electrode rotating speed in rad/s, n is the overall number of electrons transferred in oxygen reduction, F is the Faraday constant ($F = 96485 \text{ C mol}^{-1}$), C_0 is the bulk concentration of O_2 , ν is the kinetic viscosity of the electrolyte, and k is the electron-transfer constant. According to the equations above, the number of electrons transferred n and the kinetic current density j_k can be obtained from the slope and intercept of the Koutecky-Levich plots by using the values $C_0 = 1.2 \times 10^{-3} \text{ mol L}^{-1}$, $D_0 = 1.9 \times 10^{-5} \text{ cm}^2 \text{ s}^{-1}$ and $\nu = 0.01 \text{ cm}^2 \text{ s}^{-1}$.^[38]

Rotating ring-disk electrode (RRDE) voltammogram measurements were conducted on an RRDE configuration (Pine Research Instrument, USA). The disk electrode was scanned cathodically at a rate of 5.0 mV s^{-1} and the ring potential was constant at $+0.5 \text{ V}$ for oxidizing the HO_2^- intermediate. The electron transfer number n and HO_2^- intermediate production percentage ($\%\text{HO}_2^-$) were determined as followed:

$$n = \frac{4I_d}{I_d + I_r/N} \quad (4)$$

$$\%\text{HO}_2^- = \frac{200I_d/N}{I_d + I_r/N} \quad (5)$$

where I_d is disk current, I_r is ring current and N is current collection efficiency of the Pt ring which was determined to be 0.26.

Supporting Information

Supporting Information is available from the Wiley Online Library or from the author.

Acknowledgements

This work was supported by National Basic Research Program of China (973 Program, 2011CB932602) and Natural Scientific Foundation of China (No. 21306102). This is a research paper for the special issue of "Graphene Research in China".

- [1] D. S. Su, G. Q. Sun, *Angew. Chem. Int. Ed.* **2011**, *50*, 11570.
- [2] Y. Gorlin, T. F. Jaramillo, *J. Am. Chem. Soc.* **2010**, *132*, 13612.
- [3] a) B. S. Yeo, A. T. Bell, *J. Am. Chem. Soc.* **2011**, *133*, 5587; b) J. Suntivich, K. J. May, H. A. Gasteiger, J. B. Goodenough, Y. Shao-Horn, *Science* **2011**, *334*, 1383; c) Y. Y. Liang, Y. G. Li, H. L. Wang, J. G. Zhou, J. Wang, T. Regier, H. J. Dai, *Nat. Mater.* **2011**, *10*, 780; d) F. Y. Cheng, J. Chen, *Chem. Soc. Rev.* **2012**, *41*, 2172.
- [4] Y. Zhao, R. Nakamura, K. Kamiya, S. Nakanishi, K. Hashimoto, *Nat. Comm.* **2013**, *4*, 2390.
- [5] a) D. S. Yu, E. Nagelli, F. Du, L. M. Dai, *J. Phys. Chem. Lett.* **2010**, *1*, 2165; b) M. Zhang, L. M. Dai, *Nano Energy* **2012**, *1*, 514; c) H. X. Zhong, H. M. Zhang, S. S. Liu, C. W. Deng, M. R. Wang, *ChemSusChem* **2013**, *6*, 807; d) H. X. Zhong, H. M. Zhang, Z. Xu, Y. F. Tang, J. X. Mao, *ChemSusChem* **2012**, *5*, 1698; e) D. S. Su, J. Zhang, B. Frank, A. Thomas, X. C. Wang, J. Paraknowitsch, R. Schlogl, *ChemSusChem* **2010**, *3*, 169; f) Z. W. Liu, F. Peng, H. J. Wang, H. Yu, W. X. Zheng, J. A. Yang, *Angew. Chem. Int. Ed.* **2011**, *50*, 3257; g) D. S. Yu, K. L. Goh, L. Wei, H. Wang, Q. Zhang, W. C. Jiang, R. M. Si, Y. Chen, *J. Mater. Chem. A* **2013**, *1*, 11061.
- [6] R. L. Liu, D. Q. Wu, X. L. Feng, K. Mullen, *Angew. Chem. Int. Ed.* **2010**, *49*, 2565.
- [7] M. Q. Zhao, X. F. Liu, Q. Zhang, G. L. Tian, J. Q. Huang, W. C. Zhu, F. Wei, *ACS Nano* **2012**, *6*, 10759.
- [8] M. Q. Zhao, Q. Zhang, J. Q. Huang, G. L. Tian, T. C. Chen, W. Z. Qian, F. Wei, *Carbon* **2013**, *54*, 403.
- [9] D. Cai, M. Song, C. Xu, *Adv. Mater.* **2008**, *20*, 1706.
- [10] V. C. Tung, L.-M. Chen, M. J. Allen, J. K. Wassei, K. Nelson, R. B. Kaner, Y. Yang, *Nano Lett.* **2009**, *9*, 1949.
- [11] Y. Wang, Y. Wu, Y. Huang, F. Zhang, X. Yang, Y. Ma, Y. Chen, *J. Phys. Chem. C* **2011**, *115*, 23192.
- [12] a) D. S. Yu, L. M. Dai, *J. Phys. Chem. Lett.* **2010**, *1*, 467; b) T.-K. Hong, D. W. Lee, H. J. Choi, H. S. Shin, B.-S. Kim, *ACS Nano* **2010**, *4*, 3861; c) H. R. Byon, S. W. Lee, S. Chen, P. T. Hammond, Y. Shao-Horn, *Carbon* **2011**, *49*, 457.
- [13] J. J. Shao, W. Lv, Q. G. Guo, C. Zhang, Q. Xu, Q. H. Yang, F. Y. Kang, *Chem. Commun.* **2012**, *48*, 3706.
- [14] Y. G. Li, W. Zhou, H. L. Wang, L. M. Xie, Y. Y. Liang, F. Wei, J. C. Idrobo, S. J. Pennycook, H. J. Dai, *Nat. Nanotechnol.* **2012**, *7*, 394.
- [15] P. Chen, T. Y. Xiao, Y. H. Qian, S. S. Li, S. H. Yu, *Adv. Mater.* **2013**, *25*, 3192.
- [16] a) S. Chen, P. Chen, Y. Wang, *Nanoscale* **2011**, *3*, 4323; b) R. K. Paul, M. Ghazinejad, M. Penchev, J. Lin, M. Ozkan, C. S. Ozkan, *Small* **2010**, *6*, 2309; c) R. T. Lv, T. X. Cui, M. S. Jun, Q. Zhang, A. Y. Cao, D. S. Su, Z. J. Zhang, S. H. Yoon, J. Miyawaki, I. Mochida, F. Y. Kang, *Adv. Funct. Mater.* **2011**, *21*, 999;
- d) K. H. Yu, G. H. Lu, Z. Bo, S. Mao, J. H. Chen, *J. Phys. Chem. Lett.* **2011**, *2*, 1556; e) Z. J. Fan, J. Yan, L. J. Zhi, Q. Zhang, T. Wei, J. Feng, M. L. Zhang, W. Z. Qian, F. Wei, *Adv. Mater.* **2010**, *22*, 3723.
- [17] Y. Zhu, L. Li, C. G. Zhang, G. Casillas, Z. Z. Sun, Z. Yan, G. D. Ruan, Z. W. Peng, A. R. O. Raji, C. Kittrell, R. H. Hauge, J. M. Tour, *Nat. Comm.* **2012**, *3*, 1225.
- [18] Q. Zhang, J. Q. Huang, M. Q. Zhao, W. Z. Qian, F. Wei, *ChemSusChem* **2011**, *4*, 864.
- [19] a) C. L. Pint, Z. Z. Sun, S. Moghazy, Y. Q. Xu, J. M. Tour, R. H. Hauge, *ACS Nano* **2011**, *5*, 6925; b) T. Susi, J. Kotakoski, R. Arenal, S. Kurasch, H. Jiang, V. Skakalova, O. Stephan, A. V. Krasheninnikov, E. I. Kauppinen, U. Kaiser, J. C. Meyer, *ACS Nano* **2012**, *6*, 8837; c) C. M. Chen, Q. Zhang, X. C. Zhao, B. S. Zhang, Q. Q. Kong, M. G. Yang, Q. H. Yang, M. Z. Wang, Y. G. Yang, R. Schlogl, D. S. Su, *J. Mater. Chem.* **2012**, *22*, 14076.
- [20] a) S. He, Z. An, M. Wei, D. G. Evans, X. Duan, *Chem. Commun.* **2013**, *49*, 5912; b) Q. Wang, D. O'Hare, *Chem. Rev.* **2012**, *112*, 4124; c) M. Q. Zhao, Q. Zhang, J. Q. Huang, F. Wei, *Adv. Funct. Mater.* **2012**, *22*, 675.
- [21] a) M. H. Rummeli, A. Bachmatiuk, A. Scott, F. Bornert, J. H. Warner, V. Hoffman, J. H. Lin, G. Cuniberti, B. Buchner, *ACS Nano* **2010**, *4*, 4206; b) K. Xie, X. T. Qin, X. Z. Wang, Y. N. Wang, H. S. Tao, Q. Wu, L. J. Yang, Z. Hu, *Adv. Mater.* **2012**, *24*, 347; c) G. Q. Ning, Z. J. Fan, G. Wang, J. S. Gao, W. Z. Qian, F. Wei, *Chem. Commun.* **2011**, *47*, 5976.
- [22] a) J. Hwang, M. Kim, D. Campbell, H. A. Alsalman, J. Y. Kwak, S. Shivaraman, A. R. Woll, A. K. Singh, R. G. Hennig, S. Gorantla, M. H. Rummeli, M. G. Spencer, *ACS Nano* **2013**, *7*, 385; b) M. Zhou, T. Q. Lin, F. Q. Huang, Y. J. Zhong, Z. Wang, Y. F. Tang, H. Bi, D. Y. Wan, J. H. Lin, *Adv. Funct. Mater.* **2013**, *23*, 2263.
- [23] a) D. P. Wei, J. I. Mitchell, C. Tansarawiput, W. Nam, M. H. Qi, P. D. De. Ye, X. F. Xu, *Carbon* **2013**, *53*, 374; b) J. Y. Chen, Y. G. Wen, Y. L. Guo, B. Wu, L. P. Huang, Y. Z. Xue, D. C. Geng, D. Wang, G. Yu, Y. Q. Liu, *J. Am. Chem. Soc.* **2011**, *133*, 17548.
- [24] G. L. Tian, M. Q. Zhao, B. Zhang, Q. Zhang, W. Zhang, J. Q. Huang, T. C. Chen, W. Qian, D. S. Su, F. Wei, *J. Mater. Chem. A* **2013**, *2*, 1686.
- [25] M. Q. Zhao, Q. Zhang, W. Zhang, J. Q. Huang, Y. H. Zhang, D. S. Su, F. Wei, *J. Am. Chem. Soc.* **2010**, *132*, 14739.
- [26] a) G. L. Tian, M. Q. Zhao, Q. Zhang, J. Q. Huang, F. Wei, *Carbon* **2012**, *50*, 5323; b) J. Q. Huang, M. Q. Zhao, Q. Zhang, J. Q. Nie, L. D. Yao, D. S. Su, F. Wei, *Catal. Today* **2012**, *186*, 83.
- [27] J. Liang, X. Du, C. Gibson, X. W. Du, S. Z. Qiao, *Adv. Mater.* **2013**, *25*, 6226.
- [28] S. B. Yang, L. J. Zhi, K. Tang, X. L. Feng, J. Maier, K. Mullen, *Adv. Funct. Mater.* **2012**, *22*, 3634.
- [29] C. Y. He, Z. S. Li, M. L. Cai, M. Cai, J. Q. Wang, Z. Q. Tian, X. Zhang, P. K. Shen, *J. Mater. Chem. A* **2013**, *1*, 1401.
- [30] Y. Zheng, Y. Jiao, L. Ge, M. Jaroniec, S. Z. Qiao, *Angew. Chem. Int. Ed.* **2013**, *52*, 3110.
- [31] C. V. Rao, Y. Ishikawa, *J. Phys. Chem. C* **2012**, *116*, 4340.
- [32] J. D. Wiggins-Camacho, K. J. Stevenson, *J. Phys. Chem. C* **2009**, *113*, 19082.
- [33] Z. S. Wu, W. C. Ren, L. Xu, F. Li, H. M. Cheng, *ACS Nano* **2011**, *5*, 5463.
- [34] a) K. P. Gong, F. Du, Z. H. Xia, M. Durstock, L. M. Dai, *Science* **2009**, *323*, 760; b) D. S. Yu, Q. Zhang, L. M. Dai, *J. Am. Chem. Soc.* **2010**, *132*, 15127.
- [35] D. H. Deng, L. Yu, X. Q. Chen, G. X. Wang, L. Jin, X. L. Pan, J. Deng, G. Q. Sun, X. H. Bao, *Angew. Chem. Int. Ed.* **2013**, *52*, 371.
- [36] Q. Zhang, M. Q. Zhao, D. M. Tang, F. Li, J. Q. Huang, B. L. Liu, W. C. Zhu, Y. H. Zhang, F. Wei, *Angew. Chem. Int. Ed.* **2010**, *49*, 3642.
- [37] T.-C. Chen, M.-Q. Zhao, Q. Zhang, G.-L. Tian, J.-Q. Huang, F. Wei, *Adv. Funct. Mater.* **2013**, *23*, 5066.
- [38] W. Chen, S. W. Chen, *Angew. Chem. Int. Ed.* **2009**, *48*, 4386.

Received: December 2, 2013
Revised: January 3, 2014
Published online: February 27, 2014